HHS Public Access

Author manuscript

Acta Biomater. Author manuscript; available in PMC 2019 July 15.

Published in final edited form as:

Acta Biomater. 2018 July 15; 75: 213–225. doi:10.1016/j.actbio.2018.06.003.

Hybrid Collagen Alginate Hydrogel as a Platform for 3D Tumor Spheroid Invasion

Dr. Chun Liu[1], **Daniela Lewin Mejia**[1], **Benjamin Chiang**[1], **Dr. Kathryn E Luker**[1], and **Professor Gary D Luker**[1,2,3,*]

[1]Center for Molecular Imaging, Department of Radiology, University of Michigan Medical School, 109 Zina Pitcher Place, Ann Arbor, MI 48109-2200

[2]Department of Biomedical Engineering, University of Michigan Medical School

[3]Department of Microbiology and Immunology, University of Michigan Medical School

Abstract

Extracellular matrix regulates hallmark features of cancer through biochemical and mechanical signals, although mechanistic understanding of these processes remains limited by lack of models that recreate physiology of tumors. To tissue-engineer models that recapitulate three-dimensional architecture and signaling in tumors, there is a pressing need for new materials permitting flexible control of mechanical and biophysical features. We developed a hybrid hydrogel system composed of collagen and alginate to model tumor environments in breast cancer and other malignancies. Material properties of the hydrogel, including stiffness, microstructure and porosimetry, encompass parameters present in normal organs and tumors. The hydrogel possesses a well-organized, homogenous microstructure with adjustable mechanical stiffness and excellent permeability. Upon embedding multicellular tumor spheroids, we constructed a 3D tumor invasion model showing follow-the-leader migration with fibroblasts leading invasion of cancer cells similar to *in vivo*. We also demonstrated effects of CXCL12-CXCR4 signaling, a pathway implicated in tumor progression and metastasis, in a dual-tumor spheroid invasion model in 3D hydrogels. These studies establish a new hydrogel platform with material properties that can be tuned to investigate effects of environmental conditions on tumor progression, which will advance future studies of cancer cell invasion and response to therapy.

Graphical Abstract

gluker@med.umich.edu. Tel: 734-763-5476. Fax: 763-5447.

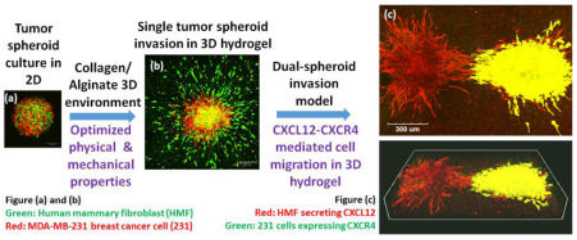

Keywords

tumor invasion; tumor spheroid; 3D model; biomaterial; hydrogel

1. Introduction

As a hallmark of cancer, metastasis is a highly complex and multi-step biological process. The first and most critical step in metastasis is migration of cancer cells away from the primary tumor through the extracellular matrix (ECM), a process called tumor invasion.[1–3] Successful cancer therapy, therefore, not only requires strategies to stop uncontrolled proliferation of malignant cells but also needs solutions to block invasion of cancer cells. Although recognized as a hallmark feature of metastasis, current understanding of biochemical and physical intercellular and cell-ECM interactions regulating cancer invasion remains incomplete [4, 5]. Challenges visualizing and experimentally controlling key steps in cancer cell migration in vivo emphasizes the need for technologies and materials to reproduce key biophysical and biochemical properties of tumor environments in vitro.

Solid tumors represent an integrated ecosystem with complex interactions among cancer cells, stromal cells, and ECM. These interactions are superimposed on local gradients of nutrients, growth factors, and oxygen in tumors.[6, 7] However, current research in cancer biology and drug discovery relies predominantly on two-dimensional (2D) cell cultures, which do not recapitulate architecture and overall environment of human tumors. Three-dimensional (3D) culture systems more closely resemble tumors in vivo, including tumor-stromal interactions, architecture, and patterns of gene expression.[8, 9] Single or multi-cellular spheroid models have emerged as a common in vitro 3D tumor model more relevant to solid tumors.[10, 11] While applied most commonly to drug testing, [12, 13] spheroids also provide relevant models for fundamental studies of tumor initiation and progression. [14–16] Investigators typically investigate spheroids cultured in aqueous media, removing cells from physiologic ECM and limiting utility of these models for studies of cancer cell invasion. To bridge the gap between 2D cell migration and in vivo metastasis, spheroids need to be integrated with functional biomaterials engineered for biomechanical and biochemical properties similar to natural ECM [17] and an adjustable 3D structure to facilitate invasion of cancer cells.

Biomaterials increasingly are utilized to develop in vitro models to study various cancer cell behaviors in simplified 3D microenvironments. However, most commonly used biomaterials for 3D models do not allow flexible control of mechanical and biophysical features.[17] Compared with synthetic materials, natural hydrogels such as collagen[18] and fibrin[19]

better resemble native tissue-like properties and thus are proposed as more relevant tumor models.[20] A drawback of these natural materials is that mechanical properties, such as stiffness and pore size, usually only can be adjusted within a narrow, controllable range.[21, 22] The limited range of tunable parameters and lack of accuracy largely limit the design flexibility of these natural materials. Crosslinkers used in these gels, either enzymatic or chemical, are also plagued by issues of cytotoxicity.[23]

Physical properties of tumor environments regulate migration and invasion of cancer cells in vivo.[24, 25] These effects on pro-metastatic functions of cancer cells can be reproduced in vitro, where several studies demonstrate that mechanical rigidity of a hydrogel regulates aggressive behaviors of cancer cells and tumor spheroids. [26–29]Changing stiffness of a hydrogel is accompanied by alterations in gel microstructure, and the consequent changes in 3D permeability affect cell viability.[22] Most current studies on applications of hydrogels in 3D cell culture only consider gel stiffness, neglecting microstructure and pore characteristics. To develop a functional 3D model mimicking tumor invasion, a biomaterial with well-characterized mechanical and physical properties is essential.

To advance studies of cancer cell invasion from 3D tumor spheroids, we designed a hybrid hydrogel system composed of collagen and alginate. By changing concentration of crosslinker, we successfully tuned the hybrid gel with a wide range of elastic moduli. We characterized 3D microstructure by scanning electron microscope (SEM) and pore size distribution and porosity with a mercury porosimeter. Upon imbedding multicellular tumor spheroids into the hybrid gel with stiffness matching human breast tumors, we successfully mimicked an early stage of breast tumor invasion, where human breast cancer cells invaded out of spheroids following human mammary fibroblasts (HMF) into the surrounding gel. We also developed a dual-spheroid invasion model to demonstrate that chemokine CXCL12 and receptor CXCR4, a signaling axis implicated in metastasis in breast cancer and more than 20 other human malignancies, [30] significantly regulate cancer cell invasion into the hydrogel system. Hence, this hybrid gel system provides a versatile platform to model biochemical and mechanical signaling in cancer, advancing knowledge of how tumor environments modulate events such as cancer cell invasion and ultimately how to block this process for cancer therapy.

2. Experimental Section

2.1. Hydrogel preparation

We prepared 50 mg/ml stock solutions of low viscosity alginic acid sodium salt (A1112, Sigma). We reconstituted 10× DMEM (D2902, Sigma) with MilliQ water and sodium bicarbonate as suggested by the supplier. To prepare hydrogels, we mixed collagen type I (Cat#50201, Ibidi) with alginate stock solution, 10× DMEM, and cell culture medium (with or without live cells and spheroids) and then adjusted to neutral pH. We then added $CaCl_2$ solution to achieve a final concentration of 3 mg/ml for collagen and 5 mg/ml for alginate. For SEM, compression testing, and porosimetry characterization, we prepared gels with different molar concentrations of $CaCl_2$ (0, 3.75, 7.5, 8.5, and 15 mM). For culturing cancer cells and tumor spheroids, we prepared gels with 7.5 mM $CaCl_2$. After mixing with $CaCl_2$,

we cured gels in a humidified tissue culture incubator with 5% CO_2 for 20 minutes at 37 °C for 20 and then added fresh cell culture medium on top.

2.2. Microstructure examination

We lyophilized hydrogel samples and mounted them on specimen stubs followed by gold sputter coating at current of 20 mA for 120 seconds. We obtained SEM images using an AMRAY 1910 field emission scanning electron microscope at 15 kV.

Mechanical compression test—We measured compressive elastic moduli of hybrid gels by compressing the hydrogels with a MicroSquisher (CellScale, Waterloo, Canada) at a constant jogging speed (4 μm/s) in a water bath. We prepared cylindrical gel samples with a diameter of 3 mm and thickness of 1 mm. Upon compression, we monitored change in gel thickness and recorded the jogging force needed generate a force-displacement curve. From these data, we determined the compressive modulus from the slope of the linear curve between stress and strain at the first 20% of strain (n = 8 samples per condition).

2.3. Porosimetry characterization

We obtained all pore structure characteristics of hydrogel samples, including pore size distribution, porosity, total pore surface area, and median pore diameter, using a MicroActive AutoPore V 9600 porosimeter (Micromeritics Instrument Corporation, Norcross, GA). We lyophilized hydrogel samples prior to intrusion. During mercury intrusion tests, we performed both low pressure (0.5–30 psi) and high pressure (30–180 psi) analyses to collect a total of 178 equilibrium pressure points. All curves shown in figure 3 are representative curves of 3 averaged tests. The data shown in figure 3c and 3d are weighted means and weighted standard deviation.

2.4. Cell culture

We cultured all cells in DMEM with 10% fetal bovine serum and 1% added penicillin/streptomycin/glutamine in a humidified 37 °C tissue culture incubator with 5% CO2. HMFs expressing CXCL12 or vector control and MDA-MB-231 human breast cancer cells (obtained from the ATCC and verified by short tandem repeat profiling) with CXCR4 or fluorescent proteins have been described previously.[31–33]

2.5. Preparation of tumor spheroids

We prepared spheroids with HMFs and MDA-MB-231 breast cancer cells as described.[34]

2.6. Fluorescence microscopy

We captured all microscopic images of cells and spheroids with an upright Olympus FVMPE-RS two photon microscope with Insight-DS+ laser (Spectra-Physics, Irvine, CA) and 25× NIR corrected objective (XLPLN25XWMP, NA=1.05, Olympus, Tokyo, Japan). We used 920 nm excitation for GFP and 1040 nm excitation for red fluorescent proteins, collecting emitted light in green (495–540 nm) and red (575–630 nm) channels, respectively. To limit signal attenuation throughout 300 μm stacks (6 μm step size), we adjusted laser power transmission to the sample and detector gain to maximize signal per slice. To capture

invasion from an entire spheroid in Figure 5 and 6, we stitched 9 images (3 by 3 square) with a resolution of 1024×1024 for each single image. To capture invasion in the dual-spheroid model shown in Figure 7, we stitched 8 images (4 by 2) with a resolution of 1024×1024 for each single image. We used the same acquisition parameters for all spheroids compared within a single experiment. For quantification of invasion distance, we captured epifluorescence images using an Olympus IX70 microscope with a 4× objective, imaging red and green channels.

2.7. Quantification of cell invasion from tumor spheroids

We defined the margin of invasion as the circular outer edge of the radial migration of cells from spheroids. To quantify invasion in Figure 6b, we took the invasive margin of MDA-MB-231 cells in gels as a circle and then measured the diameter using cellSens software (Olympus, Tokyo, Japan). For Figure 7b, we measured the horizontal distance between the invasion margin of 231 cells and the center of HMF spheroid daily and normalized values to the distance on day 0. For all experiments, we used 6 spheroids per condition for each replicate and performed 5 independent biologic replicates.

2.8. Statistical analysis

We report all statistics as means ± standard deviation. We used ANOVA tests followed by the Tukey test for post-hoc pairwise comparisons.

3. Results and discussion

3.1. Mechanical properties of Col/Algi hybrid gel

Sodium alginate in aqueous solutions forms a hydrogel by divalent calcium binding.[35] Similarly, mechanical properties of the Col/Algi hybrid gels also can be tuned by altering the concentration of $CaCl_2$, which crosslinks the alginate. As shown in Figure 1a, increasing the molar concentration of $CaCl_2$ from 3.75 to 15 mM increased gel stiffness from 1221±92 to 9870±654 Pa (Young's modulus) as measured by compression tests in a hydrated condition. Such variation in elastic modulus is broad enough to encompass the stiffness of several soft organs, including healthy and malignant tissues.[36, 37] Note that 1200 Pa corresponds to the elastic moduli of stroma tissue attached to tumor (918±269Pa), while 4000 Pa corresponds to that of an average tumor (4049±938 Pa).[38]

The gel system developed in this study classifies as a hydrogel, a solid containing water-swollen, crosslinked, hydrophilic polymer. We performed mechanical compression testing in a water bath to avoid water loss, which can significantly affect the mechanical behavior of hydrogels. In a hydrated state, our hydrogel behaves similarly to rubber-like materials, which can be analyzed using theories of rubber elasticity.[39] Similar to other rubber-like materials, the mechanical behavior of the hydrogel in this study is mainly determined by the architecture of the hybrid polymer network of collagen and alginate. Figure 1b shows a representative linear region of stress-strain curve for gels crosslinked by 7.5 mM $CaCl_2$, which demonstrates line fitting with R^2 of 0.9987.

Viscoelasticity is another model commonly used to examine mechanical behavior of hydrogels, where dynamic mechanical analysis (DMA) and rheometry data frequently are reported as a plot of storage and loss moduli versus angular frequency.[40] However, without further analysis, those dynamic results have shown little success to explicitly describe or predict real gel stiffness. In our study, the gel only shows viscoelastic behavior during gelation as temperature elevates from 4 to 37 °C. Once the gel is cured, it behaves more like a solid than viscous fluid. Therefore, Young's modulus is more appropriate to characterize our gel than storage modulus.

There are also other theoretical models specially developed to address the hydrogel mechanical properties.[41–43] Since the hydrogel can be taken as a multiphasic material involving both solid network and liquid phase, the overall mechanical compression of a hydrogel can be decoupled into two components: flux of liquid out of the gel system and deformation of the network. Stress-relaxation tests have been applied with a corresponding stress strain equilibrium, illustrating true mechanical properties of the bulk material.[42] In this study, we focused on the stiffness that live cells experience. Therefore, we performed the compression test in a water bath to maintain the hydrogel at a saturated condition, and only considered the elastic region of stress-strain curve at a fixed jogging speed of 4 μm/s. The hydrogel showed elastic behavior with strain less than 30%, and relaxation testing demonstrated hydrogels fully recover the original thickness within one minute during relaxation.

The gel system developed in this study allowed us to control stiffness without altering the major gel components, since the concentration of alginate and collagen in the gel remain constant. The change in degree of calcium crosslinking does not affect the number of cell adhesion motifs on the collagen network. Previous studies have manipulated mechanical rigidity of collagen gels by varying collagen concentration and suggested that the stiffness change in a 3D collagen gel determines aggressive behaviors of cancer cells.[21, 44] However, changes in collagen concentration not only alter gel stiffness but also alter gel permeability and number of cell binding sites, which complicates analysis of cell-matrix interactions. Tumors with well-defined collagen networks resist penetration by macromolecular drugs.[41] Our gel system overcomes these limitations by controlling stiffness of a 3D environment with well-defined network while minimizing confounding variables.

3.2. Microstructure changes with calcium crosslinking

Figure 2a shows the internal microstructure of hydrogels with different degrees of calcium crosslinking. After freeze drying, we cut gel samples into pieces and mounted them on the specimen stub with the cross section facing up to avoid the polymeric "skin" on the outer surface as described in literature.[45] In accordance with previous studies, the microstructure of collagen appeared to be a fibrillary network,[46] while the microstructure of alginate looked more like interconnected curved flakes.[47] Images with high magnification (1500×) revealed the relationship between collagen fibrils and alginate flakes after mixing and curing. Compared with the control gel (0 mM $CaCl_2$), increased calcium

content crosslinked more alginate, resulting in greater attachment of alginate flakes onto collagen fibrils to form large curved, sheet-like structures.

SEM images of medium magnification (500×) revealed pore geometry and apparent pore size according to specific locations in the hydrogel. While the 0 mM $CaCl_2$ gel showed a large degree of randomness in pore size and geometry, calcium crosslinked gels clearly displayed well-organized pore structure. Regarding pore geometry, the gels crosslinked with 3.75, 5, and 7.5 mM $CaCl_2$ exhibited more pores in round shape, while the gels with 8.5 and 15 mM $CaCl_2$ contained more pores with a flat compressed shape. Changes in pore geometry by calcium crosslinking revealed a competitive relationship between collagen and alginate in dominating the overall microstructure. When crosslinking of only a small amount of alginate flakes, the collagen fibril network dominated the pore structure. Accordingly, most of the free alginate flakes randomly wrapped onto the collagen backbones, resulting in round pores. As the calcium content increased, more of the alginate monomers crosslinked and dominated the gel structure. Therefore, the 15mM $CaCl_2$ gel sample resembled stacks of large, flattened sheets.

Low magnification (250×) images provided relevant information about homogeneity and heterogeneity of the overall hydrogel network. Gels with $CaCl_2$ concentrations above 5 mM all showed homogenous microstructure with well-organized pores. The 3.75 mM gel sample exhibited less homogeneity compared with other samples and more closely resembled heterogeneity of the 0 mM gel sample. To summarize, calcium crosslinking of alginate modulated the microstructure of the hybrid gel system with increasing concentrations of calcium changing pore geometry from round to flat.

Figure 2b shows fluorescent images of a blank 7.5 mM CaCl2 gel under hydrated condition with different magnifications. The rhodamine-tagged alginate molecules are shown in red, while collagen fibers stained with a FITC-tagged probe are shown in green. Yellow on both images shows a perfect overlay of red and green, indicating the co-localization of alginate with collagen. This further confirmed results in Figure 2a, where alginate flakes attach and wrapped onto collagen fibers to form the microstructure.

3.3. Characterization of gels by porosimetry

SEM images above revealed the microstructure change with calcium crosslinking. However, thos images did not clearly define pore size and porosity change since our hydrogel system contained a complicated hierarchy of pores. Although pore size analysis based on SEM images has been applied in previous studies,[48, 49] thresholding 2D binary images is inaccurate.[50] To fully understand the inner structure of our gel while avoiding bias, we employed mercury intrusion porosimetry (MIP) to provide more comprehensive analysis of pore characteristics. The mercury porosimetry analysis technique is based on the intrusion of mercury into a porous structure under precisely controlled pressure gradients. Since mercury is considered as the best non-wetting liquid that does not enter pores by capillary action, the volume of mercury entering the pore spaces can be directly related to the pressure applied externally. The pore size is inversely proportional to the applied pressure, and the volume of pores can be calculated based on Washburn’s equation. Pore size distribution can be illustrated by mercury intrusion profile (MIP). The MIP approach has been widely applied

for not only the pore size and porosity measurement, but also for other pore structure characteristics such as pore surface area and median pore diameter. The range of pore-throat size it can investigate is wide, normally from ~3 nm up to ~500 μm.[51, 52]

Figure 3a shows changes in cumulative pore area with pore size for gels with different degrees of crosslinking. The x-axis is the pore size diameter in reverse manner, indicating the pores with larger diameter contribute more to the cumulative pore area as compared to smaller pores. The content of $CaCl_2$ in the gel changed the curve in an “up-to-down” manner. From 3.75 to 7.5 mM the cumulative pore area increased with calcium content; once the 7.5 mM gel reached the top, the curve then dropped as calcium content further increased to 15 mM. The control gel, however, did not follow this trend and traversed all the curves with calcium content. This is in accordance with SEM images, where the control gel did not exhibit a homogenous microstructure. In combination with SEM images of 7.5, 8.5, and 15 mM gels, the cumulative pore area decreased as the pore shape of changes from round to compressed.

Figure 3b shows the pore size distribution of each gel. The log differential intrusion on y-axis indicates the volume of mercury intruded into pores. Therefore, the peak on the curve defines the diameter at which the largest volume of pores exists. Relative to curves with various concentrations of calcium, the curve for the control gel displayed a flat shape across the x-axis with a moderate peak, indicating the gel without calcium crosslinking possessed a random distribution of pore diameters. The peaks of curves with calcium crosslinking basically occurred at a similar range of pore size (100±30 μm), indicating similar pore size distribution. However, the overall pore volume (area under each intrusion curve) showed a similar trend to figure 3a, where the 7.5 mM gel was the highest and the 3.75 mM gel was lowest. Note that a few small, sharp peaks occurred at pore sizes below 10,000 nm, which are known as yield peaks indicating the collapse of pores due to high pressure.

The average and median pore sizes of each gel are shown in Figure 3c. The median pore size according to pore volume was larger than the median pore size according to pore area, which means larger pores contribute more to the volume and smaller pores contribute more to the area. The curve of average pore size falls in between the curves of two medians. We identified no significant difference in average and median pore size based on changes in calcium concentration, confirming a similar distribution of pore size for all gels with calcium crosslinking.

Porosity of gels measured by mercury intrusion is shown in Figure 3d, where the 7.5 mM and 15 mM $CaCl_2$ gels exhibit highest and lowest values, respectively. This result can be explained by the microstructure changes shown in Figure 2. As the content of calcium increases from 7.5 to 15 mM, the crosslinked alginate flakes dominated the overall structure and changed the pore geometry from round to flat. Tiny pores formed mainly from the collagen network disappeared, as evidenced by the rise of median pore sizes according to area at 15 mM on Figure 3c. Therefore, loss to tiny pores attenuated overall porosity of 15 mM gel. The compressed pore geometry also contributed to the shift of the peak of 15 mM curve in Figure 3b, which exhibited a relatively sharper shape at diameters below 100,000 nm as compared with other curves.

As a well-established technique for characterization of porous material, MIP has several advantages over other pore structure characterization methods, including a wide range of measurable pore size from nano- to micro-scale and high accuracy. The fundamental data generated from this technique can also indicate various pore characteristics and physical properties. However, several key parameters need to be considered to achieve convincing results. First, the sample mass and volume are significant for the calculation of mercury intrusion. Variance in sample mass affects the calculated results of pore volume and porosity. Therefore, instead of using normal averages, we applied weighted means of total mercury intrusion volume for three replicates of each gel type to generate the pore size distribution curves in Figure 3a and 3b. We also represented the average and median pore sizes as well as porosity numbers by weighted means and weighted standard deviations as shown in Figure 3c and 3d. In addition, the pressure gradient also highly affects the measurement. Since the freeze-dried hydrogels are brittle, a sharp gradient will easily destroy all the inner pore structures. We therefore first applied a low-pressure cycle (0.5–30 psi) to slowly saturate the macro-pores, followed by a high pressure (30–180 psi) cycle to further push mercury into nano-pores.

To summarize, the gel system developed in this study exhibited a wide pore size distribution and large porosity. The large pore size and porosity contributed to good permeability of the hydrogel, as well as excellent penetration by cells. To our knowledge, this is the first study to address effects of calcium crosslinking on hydrogel pore size distribution and porosity in such a systematic way. The 7.5 mM $CaCl_2$gel has the largest pore area and volume with a median pore size of 95 μm by volume and 93% porosity, making this gel the most promising for invasion of cancer cells. Next, we specially tested cancer cell growth and tumor spheroid invasion in the gel with 7.5 mM $CaCl_2$.

3.4. Cancer cells proliferate in hybrid gel system

We cultured MDA-MB-231 human breast cancer cells, a highly invasive basal subtype of breast cancer, in the hydrogel for 7 days. Figure 4 displays cell morphologies after one and seven days of culture. We seeded 231 cells stably expressing fluorescent protein mKate (shown as red in images) at the same density (50,000 cells/ml) for both 2D and 3D culture. Presented images for 3D culture represent maximum intensity in z-projection over a depth of 300 μm. Different from 2D culture where 231 cells show flat and round morphology (Figure 4a and 4e), cells in the 3D gel tend to elongate and extend fine protrusions in different directions. After seven days of culture in hydrogel, 231 cells formed clusters in 3D, and the clusters connected to each other through cell protrusions. We did not observe notable differences in cell morphology among gels with different calcium crosslinking. Changes in concentration of gel components (collagen or alginate concentration) may alter cell proliferation due to the changes in gel mechanical properties. However, we did not identify any negative effect on cell viability in this hydrogel system. To summarize, our gel system successfully induced 231 cells to show morphology associated with invasion.

3.5. Tumor spheroid invasion in hybrid gel system

Next, we tested invasion of cells from multicellular tumor spheroids in our hybrid hydrogel system. We previously have established methods to rapidly form spheroids combining

cancer and stromal cells in low adhesion 384 well plates.[34, 53] We embedded multicellular spheroids composed of human mammary fibroblasts (HMFs) and MDA-MB-231 cancer cell into Col/Algi gels with 7.5 mM $CaCl_2$ content. As a control, we also embedded spheroids into a standard collagen gel with no alginate. Figure 5 shows the morphology of spheroids on day 0 before embedding (Figure 5a and 5b), and after six days in the Col/Algi gel (5c and 5d). Figure 5(e–f) shows the same type of spheroid cultured in standard collagen gel for six days. HMFs and MDA-MB-231 cells stably express GFP and mKate fluorescent proteins, respectively. On day 0, the spheroid was a compact mixture of green (HMFs) and red (MDA-MB-231) cells with ~ 300 μm diameter. After six days in the hybrid hydrogel, the spheroids showed clear invasion into the surrounding gel with a diameter of overall invasion margin of approximately 1200 μm. While the core of a spheroid retains a mixture of HMFs and MDA-MB-231 cells (shown as yellow color as an overlay of red and green), cancer cells migrated out of the spheroid, radiating outward and forming a red ring surrounding the core. Moreover, HMFs moved much further away from the spheroid, orienting in a sun-burst pattern and invading a large volume of the surrounding gel. As compared with our hybrid hydrogel, the spheroid in standard collagen gel grew with time (~800 μm in diameter on day 6) but showed very limited invasion into the surrounding gel. Instead of sun-burst migration of both HMF and cancer cells, the spheroid in standard collagen gel stayed intact over time with invasion of only the HMFs at the spheroid edge. Differences in invasion may due to the microstructure difference between a hybrid Col/Algi gel and standard collagen gel. Our hybrid hydrogel showed well-defined microstructure with large pore size as shown in Figure 2 and 3, which facilitate migration of cells. We also verified this tumor invasion model using other recipes of Col/Algi gel with a fixed collagen concentration of 3mg/ml (to keep cell binding sites constant) and varied alginate (5mg/ml–20mg/ml) and calcium concentrations (3.75mM to 30mM). All gel recipes showed cancer cell migration as well as tumor spheroid invasion to different extents (data not shown).

Cultures of tumor spheroids in medium cannot reproduce complex interactions among tumor cells, stromal cells, and ECM that are relevant for invasion. The current 3D invasion model demonstrates interaction between HMFs and cancer cells early in invasion, where HMFs migrate further than cancer cells and make the way for them to follow. This pattern of follow-the-leader migration in cancer with fibroblasts leading invasion of cancer cells has been observed in vivo,[54] providing further evidence that our hydrogel system reproduces physiology of cancer cell invasion in tumors. Until recently, only a few research groups have studied invasion of tumor spheroids in a 3D hydrogel system, while most of studies on spheroids focused on testing potency and efficacy of new drugs.[10, 55–57] To our knowledge, this is the first study showing that HMFs lead the way for breast cancer cells in a 3D hydrogel that mimics an early stage of tumor invasion.

3.6. CXCL12-CXCR4 signaling regulates invasion of breast cancer cells

In breast cancer, CXCL12 (also known as SDF-1) is secreted by both carcinoma-associated fibroblasts and cancer cells in the primary tumor environment and common sites of metastasis.[7, 30, 58] Binding of CXCL12 to receptor CXCR4 correlates highly with metastatic properties of breast cancer cells, as CXCR4 commonly is upregulated on breast cancer cells.[59] Developing 3D models to understand CXCL12-CXCR4 signaling in cancer

cell invasion will advance ongoing efforts to target this pathway in breast cancer and other malignancies.

We previously have shown migration of breast cancer cells expressing CXCR4 towards CXCL12 secreting cells in a surface template hydrogel with droplets of collagen gel incorporated with cells patterned on PDMS-PAA surface.[60] In the current study, we formed tumor spheroids with HMFs secreting CXCL12 and MDA-MB-231 cells expressing CXCR4 (MDA-MB-231-X4) and then embedded spheroids in the 7.5 mM $CaCl_2$ hydrogel. As controls we used spheroids combining HMFs that do not secrete CXCL12 with MDA-MB-231 cells lacking CXCR4 (231(WT)/HMF(WT); 231(X4)/HMF(WT); and 231(WT)/HMF(CXCL12). We quantified invasion of cancer cells into the adjacent gel for all conditions. Figure 6a shows morphologies of spheroids with different components after one day (top left corner) and 5 days in culture in gels. To enable comparisons of different cells, we pseudo-colored cells as follows: HMF(CXCL12), red; HMF(WT), yellow; 231(X4), green; and 231(WT), cyan. Similar to figure 5, cells from all spheroids invaded into the gel in a sun-burst pattern after five days of culture, where HMF cells invade and lead the way for cancer cells. However, for the 231(X4)/HMF(CXCL12) spheroid, cancer cells invaded significantly less than other groups (Figure 6b). Since CXCL12-CXCR4 signaling increases adhesion of cancer cells,[61, 62] we postulate this signaling pathway promotes intercellular adhesion within spheroids that reduce cell invasion in the absence of an external gradient of CXCL12. Our hydrogel system provides a facile model system to investigate mechanisms controlling CXCL12-CXCR4-mediated adhesion versus invasion toward chemokine gradients.

To further quantify CXCL12-CXCR4 mediated invasion, we next placed two spheroids with a relatively large distance (approximately 1 mm from center to center) in the same hydrogel. One spheroid consisted of HMFs that secrete CXCL12, while the other spheroid combined MDA-MB-231-X4 cells and wild-type HMFs. As shown in Figure 7a, both spheroids were round and separated by blank gel on day 0. Cancer cells began invading into the surrounding gel on day one, while both spheroids showed a sun-burst pattern of invasion on day 3. Migration of cells out of spheroids showed anisotropic distribution with cells closing the gap between spheroids, unlike isotropic distribution of cells migrating from a single spheroid in Figures 5 and 6. This bridge became clear and obvious on day four, where HMFs and 231 cells finally filled the entire gap between spheroids. A 3D view on day 4 showed the connection was not just confined to one focal plane but extended throughout the gel. As a control, we placed spheroids of HMFs wild-type and spheroid of MDB-MB-231 wild-type cells and HMF wild-type in the same gel. The bottom row of Figure 7a shows images of the WT group. Instead of showing anisotropic migration, the wild-type spheroids invaded the gel in an isotropic sun-burst pattern, similar to Figure 6 and did not form a bridge between spheroids as we observed with combinations of CXCL12-CXCR4 spheroids. We quantified the horizontal length from the invasive margin of cancer cells to the center of HMF spheroids for three days to illustrate the distance from 231 cells to the targeted destination and normalized measurements to the original distance on day 0 in Figure 7b. Both the CXCL12-CXCR4 group and WT-WT group showed similar invasion on day one, while the two curves progressively diverged on days two and four, respectively. The distance in the CXCL12-CXCR4 group was significantly smaller than the WT-WT group, indicating that

CXCL12-CXCR4 signaling significantly induced directional migration of 231 cells in this dual-spheroid model. Since we demonstrated that HMF with CXCL12 secretion influenced migration of 231-X4 cancer cells in Figure 6, in Figure 7 we used this dual spheroid invasion model to further demonstrate that CXCL12-CXCR4 signaling induced directional cell migration in this 3D hydrogel environment. 231-X4 cells migrated together with wild-type HMF towards HMFs secreting CXCL12. As shown in the day four image, wild-type HMFs also connected with HMF secreting CXCL12 in the bridge between spheroids, which overlapped extensively with 231-X4 cells. Combined with results from Figure 5 and 6, we conclude that the crosstalk between HMF and cancer cells determines directionality of tumor invasion. Without an external chemotactic gradient, cancer cells followed the track of HMFs, resulting an isotropic invasion. If the gradient of CXCL12 localized inside the spheroid, then cancer cell invasion was limited. Conversely, a chemotactic gradient of CXCL12 in the surrounding gel stimulated cancer cells to migrate along with HMF in the direction of the gradient.

The 3D hybrid hydrogel system we developed has several practical advantages over commercially available 3D gels, such as Matrigel and pure collagen. First, non-crosslinked collagen as a predominant component of the tumor ECM provides extensive cell binding sites and interaction with multiple growth factors without toxic crosslinkers. Second, alginate as a structural support of the gel offers adjustable mechanical properties as well as homogeneous pore characteristics to enhance cell migration. Third, the blank gel system possesses great stability in a hydrated condition over six months, and the gel persists and maintains viable cells for at least a month. All these features make our Col/Algi hydrogel a highly attractive platform for in vitro modeling of tumor invasion and enable applications to study cancer cell migration towards chemokine gradients in a controlled fashion.

ECM changes over time during tumor progression with upregulation of proteins such as fibronectin and hyaluronic acid and remodeling of existing proteins by invading cancer cells and associated stromal cells.[63, 64] In our current hydrogel model, HMFs and breast cancer cells migrated along the same tracks oriented radially to embedded spheroids, suggesting reorganization of the matrix network and tumor-stromal interactions in invasion. This result corresponds with the recent finding that HMFs produce and align a fibronectin rich ECM network to promote directional migration of cancer cells.[65] Stromal fibroblasts in tumors exert mechanical forces to remodel collagen around tumors in vivo, producing radially aligned collagen fibers at the interface of a primary tumor and ECM, promoting invasion of cancer cells into adjacent tissue.[66] The Col/Algi hydrogel developed in this research positions us to further investigate and define the complex interplay among multiple parameters, including gradients of chemokines, intercellular interactions, and cytoskeletal and ECM remodeling, that drive cancer cell invasion in metastasis.

We note the hydrogel system can be modified to include other cellular and structural stromal components of tumors ECM, such as HA, fibronectin, and other glycosaminoglycans. In addition to collagen fibers, aligned fibronectin enhances migration and invasion of cancer cells.[65] Deposition of glycosaminoglycans, such as hyaluronic acid (HA), correlates with tumor progression and poor prognosis.[67, 68] HA facilitates migration of cancer cells by establishing openings in adjacent ECM and binding chemokines to generate haptotactic

gradients.[68] In addition, invasion models demonstrated in this study can be tuned to adapt different conditions present in tumor environments, providing tremendous potential to expand current knowledge of chemical, cell–cell, cell–ECM, and mechanical cues in tumor invasion.

4. Conclusion

We constructed a 3D tumor invasion platform using a hybrid hydrogel composed of collagen and alginate. The hydrogel possesses a well-organized microstructure with adjustable mechanical stiffness and excellent permeability. Upon imbedding multicellular tumor spheroids, this biomimetic tumor environment provides a valuable new tool to simulate key steps in tumor invasion. Moreover, we also demonstrated effects of chemokine signaling in tumor spheroids and invasion in 3D. Insights from future studies using this model will facilitate mechanistic studies of how environmental conditions regulate cancer progression and response to therapy.

Acknowledgments

This work was supported by United States National Institutes of Health grants R01CA196018 and U01CA210152. We thank the University of Michigan Biointerfaces Institute for use of facilities. We thank Chris Edwards, Jeff Harrison, and the University of Michigan Microscopy & Image Analysis Laboratory Core for help with SEM imaging.

References

1. Chambers AF, Groom AC, MacDonald IC. Dissemination and growth of cancer cells in metastatic sites. Nature Rev Cancer. 2002; 2:563–572. [PubMed: 12154349]
2. Clark AG, Vignjevic DM. Modes of cancer cell invasion and the role of the microenvironment. Curr Opin Cell Biol. 2015; 36:13–22. [PubMed: 26183445]
3. Friedl P, Wolf K. Tumour-cell invasion and migration: diversity and escape mechanisms. Nature Rev Cancer. 2003; 3:362–374. [PubMed: 12724734]
4. Bissell MJ, Hines WC. Why don’t we get more cancer? A proposed role of the microenvironment in restraining cancer progression. Nat Med. 2011; 17(3):320–329. [PubMed: 21383745]
5. Katt ME, Placone AL, Wong AD, Xu ZS, Searson PC. In Vitro Tumor Models: Advantages, Disadvantages, Variables, and Selecting the Right Platform. Front Bioeng Biotechnol. 2016; 4:12. [PubMed: 26904541]
6. Mao Y, Keller ET, Garfield DH, Shen K, Wang J. Stromal cells in tumor microenvironment and breast cancer. Cancer and Metastasis Reviews. 2013; 32(1):303–315. [PubMed: 23114846]
7. Muller A. Involvement of chemokine receptors in breast cancer metastasis. Nature. 2001; 410:50–56. [PubMed: 11242036]
8. Kenny PA, Lee GY, Myers CA, Neve RM, Semeiks JR, Spellman PT, Lorenz K, Lee EH, Barcellos-Hoff MH, Petersen OW, Gray JW, Bissell MJ. The morphologies of breast cancer cell lines in three-dimensional assays correlate with their profiles of gene expression. Molecular oncology. 2007; 1(1): 84–96. [PubMed: 18516279]
9. Muthuswamy SK. 3D culture reveals a signaling network. Breast Cancer Research: BCR. 2011; 13(1):103–103. [PubMed: 21349209]
10. Nath S, Devi GR. Three-dimensional culture systems in cancer research: Focus on tumor spheroid model. Pharmacol Ther. 2016; 163:94–108. [PubMed: 27063403]
11. Hirschhaeuser F, Menne H, Dittfeld C, West J, Mueller-Klieser W, Kunz-Schughart LA. Multicellular tumor spheroids: An underestimated tool is catching up again. Journal of Biotechnology. 2010; 148(1):3–15. [PubMed: 20097238]

12. Sant S, Johnston PA. The production of 3D tumor spheroids for cancer drug discovery. Drug Discovery Today: Technologies. 2017; 23:27–36. [PubMed: 28647083]
13. Zanoni M, Piccinini F, Arienti C, Zamagni A, Santi S, Polico R, Bevilacqua A, Tesei A. 3D tumor spheroid models for in vitro therapeutic screening: a systematic approach to enhance the biological relevance of data obtained. Sci Rep. 2016; 6:19103. [PubMed: 26752500]
14. Kim SA, Lee EK, Kuh HJ. Co-culture of 3D tumor spheroids with fibroblasts as a model for epithelial–mesenchymal transition in vitro. Experimental Cell Research. 2015; 335(2):187–196. [PubMed: 26022665]
15. Liu T, Lin B, Qin J. Carcinoma-associated fibroblasts promoted tumor spheroid invasion on a microfluidic 3D co-culture device. Lab Chip. 2010; 10(13):1671–7. [PubMed: 20414488]
16. Fischbach C, Chen R, Matsumoto T, Schmelzle T, Brugge JS, Polverini PJ, Mooney DJ. Engineering tumors with 3D scaffolds. Nat Meth. 2007; 4(10):855–860.
17. Mano JF. Designing biomaterials for tissue engineering based on the deconstruction of the native cellular environment. Materials Letters. 2015; 141:198–202.
18. Szot CS, Buchanan CF, Freeman JW, Rylander MN. 3D in vitro bioengineered tumors based on collagen I hydrogels. Biomaterials. 2011; 32(31):7905–7912. [PubMed: 21782234]
19. Liu J, Tan Y, Zhang H, Zhang Y, Xu P, Chen J, Poh YC, Tang K, Wang N, Huang B. Soft fibrin gels promote selection and growth of tumorigenic cells. Nat Mater. 2012; 11(8):734–741. [PubMed: 22751180]
20. Provenzano PP, Eliceiri KW, Campbell JM, Inman DR, White JG, Keely PJ. Collagen reorganization at the tumor-stromal interface facilitates local invasion. BMC Medicine. 2006; 4(1): 38. [PubMed: 17190588]
21. Griffith LG, Swartz MA. Capturing complex 3D tissue physiology in vitro. Nat Rev Mol Cell Biol. 2006; 7(3):211–224. [PubMed: 16496023]
22. Cha C, Kim SY, Cao L, Kong H. Decoupled control of stiffness and permeability with a cell-encapsulating poly(ethylene glycol) dimethacrylate hydrogel. Biomaterials. 2010; 31(18):4864–4871. [PubMed: 20347136]
23. Delgado LM, Bayon Y, Pandit A, Zeugolis DI. To Cross-Link or Not to Cross-Link? Cross-Linking Associated Foreign Body Response of Collagen-Based Devices, Tissue Engineering. Part B, Reviews. 2015; 21(3):298–313. [PubMed: 25517923]
24. Bissell MJ, Kenny PA, Radisky DC. Microenvironmental Regulators of Tissue Structure and Function Also Regulate Tumor Induction and Progression: The Role of Extracellular Matrix and Its Degrading Enzymes. Cold Spring Harbor symposia on quantitative biology. 2005; 70:343–356. [PubMed: 16869771]
25. Hynes RO. Extracellular matrix: not just pretty fibrils. Science (New York, NY). 2009; 326(5957): 1216–1219.
26. Schedin P, Keely PJ. Mammary Gland ECM Remodeling, Stiffness, and Mechanosignaling in Normal Development and Tumor Progression. Cold Spring Harbor Perspectives in Biology. 2011; 3(1)
27. Taubenberger AV, Bray LJ, Haller B, Shaposhnykov A, Binner M, Freudenberg U, Guck J, Werner C. 3D extracellular matrix interactions modulate tumour cell growth, invasion and angiogenesis in engineered tumour microenvironments. Acta Biomater. 2016; 36:73–85. [PubMed: 26971667]
28. Ulrich TA, de Juan Pardo EM, Kumar S. The mechanical rigidity of the extracellular matrix regulates the structure, motility, and proliferation of glioma cells. Cancer research. 2009; 69(10): 4167–4174. [PubMed: 19435897]
29. Liang Y, Jeong J, DeVolder RJ, Cha C, Wang F, Tong YW, Kong H. A cell-instructive hydrogel to regulate malignancy of 3D tumor spheroids with matrix rigidity. Biomaterials. 2011; 32(35):9308–15. [PubMed: 21911252]
30. Luker KE, Luker GD. Functions of CXCL12 and CXCR4 in breast cancer. Cancer Letters. 2006; 238(1):30–41. [PubMed: 16046252]
31. Song JW, Cavnar SP, Walker AC, Luker KE, Gupta M, Tung YC, Luker GD, Takayama S. Microfluidic Endothelium for Studying the Intravascular Adhesion of Metastatic Breast Cancer Cells. Plos One. 2009; 4(6):e5756. [PubMed: 19484126]

32. Cavnar SP, Ray P, Moudgil P, Chang SL, Luker KE, Linderman JJ, Takayama S, Luker GD. Microfluidic source-sink model reveals effects of biophysically distinct CXCL12-isoforms in breast cancer chemotaxis. Integrative biology: quantitative biosciences from nano to macro. 2014; 6(5):564–576. [PubMed: 24675873]
33. Luker KE, Lewin SA, Mihalko LA, Schmidt BT, Winkler JS, Coggins NL, Thomas DG, Luker GD. Scavenging of CXCL12 by CXCR7 Promotes Tumor Growth and Metastasis of CXCR4-positive Breast Cancer Cells. Oncogene. 2012; 31(45):4750–4758. [PubMed: 22266857]
34. Cavnar SP, Rickelmann AD, Meguiar KF, Xiao A, Dosch J, Leung BM, Cai Lesher-Perez S, Chitta S, Luker KE, Takayama S, Luker GD. Modeling Selective Elimination of Quiescent Cancer Cells from Bone Marrow. Neoplasia. 2015; 17(8):625–633. [PubMed: 26408255]
35. Smidsrød O, Skjåk-Brælk G. Alginate as immobilization matrix for cells. Trends in Biotechnology. 1990; 8:71–78. [PubMed: 1366500]
36. Handorf AM, Zhou Y, Halanski MA, Li WJ. Tissue Stiffness Dictates Development, Homeostasis, and Disease Progression. Organogenesis. 2015; 11(1):1–15. [PubMed: 25915734]
37. Cox TR, Erler JT. Remodeling and homeostasis of the extracellular matrix: implications for fibrotic diseases and cancer. Disease Models & Mechanisms. 2011; 4(2):165–178. [PubMed: 21324931]
38. Paszek MJ, Zahir N, Johnson KR, Lakins JN, Rozenberg GI, Gefen A, Reinhart-King CA, Margulies SS, Dembo M, Boettiger D, Hammer DA, Weaver VM. Tensional homeostasis and the malignant phenotype. Cancer Cell. 8(3):241–254.
39. Anseth KS, Bowman CN, Brannon-Peppas L. Mechanical properties of hydrogels and their experimental determination. Biomaterials. 1996; 17(17):1647–1657. [PubMed: 8866026]
40. Oyen ML. Mechanical characterisation of hydrogel materials. International Materials Reviews. 2014; 59(1):44–59.
41. Netti PA, Berk DA, Swartz MA, Grodzinsky AJ, Jain RK. Role of Extracellular Matrix Assembly in Interstitial Transport in Solid Tumors. Cancer Research. 2000; 60(9):2497. [PubMed: 10811131]
42. Urciuolo F, Imparato G, Netti PA. Effect of dynamic loading on solute transport in soft gels implication for drug delivery. AIChE Journal. 2008; 54(3):824–834.
43. Mow VC, Holmes MH, Michael Lai W. Fluid transport and mechanical properties of articular cartilage: A review. Journal of Biomechanics. 1984; 17(5):377–394. [PubMed: 6376512]
44. Butcher DT, Alliston T, Weaver VM. A tense situation: forcing tumour progression. Nat Rev Cancer. 2009; 9(2):108–122. [PubMed: 19165226]
45. Ferreira L, Figueiredo MM, Gil MH, Ramos MA. Structural analysis of dextran-based hydrogels obtained chemoenzymatically. Journal of Biomedical Materials Research Part B: Applied Biomaterials. 2006; 77B(1):55–64.
46. Miron-Mendoza M, Seemann J, Grinnell F. The differential regulation of cell motile activity through matrix stiffness and porosity in three dimensional collagen matrices. Biomaterials. 2010; 31(25):6425–6435. [PubMed: 20537378]
47. Jang J, Seol YJ, Kim HJ, Kundu J, Kim SW, Cho DW. Effects of alginate hydrogel cross-linking density on mechanical and biological behaviors for tissue engineering. Journal of the Mechanical Behavior of Biomedical Materials. 2014; 37:69–77. [PubMed: 24880568]
48. Zhang YN, Avery RK, Vallmajo-Martin Q, Assmann A, Vegh A, Memic A, Olsen BD, Annabi N, Khademhosseini A. A Highly Elastic and Rapidly Crosslinkable Elastin-Like Polypeptide-Based Hydrogel for Biomedical Applications. Advanced functional materials. 2015; 25(30):4814–4826. [PubMed: 26523134]
49. Lee PF, Bai Y, Smith RL, Bayless KJ, Yeh AT. Angiogenic responses are enhanced in mechanically and microscopically characterized, microbial transglutaminase crosslinked collagen matrices with increased stiffness. Acta Biomaterialia. 2013; 9(7):7178–7190. [PubMed: 23571003]
50. Lubelli B, de Winter DAM, Post JA, van Hees RPJ, Drury MR. Cryo-FIB–SEM and MIP study of porosity and pore size distribution of bentonite and kaolin at different moisture contents. Applied Clay Science. 2013; 80:358–365.
51. Zhang N, He M, Zhang B, Qiao F, Sheng H, Hu Q. Pore structure characteristics and permeability of deep sedimentary rocks determined by mercury intrusion porosimetry. Journal of Earth Science. 2016; 27(4):670–676.

52. Anovitz LM, Cole DR. Characterization and Analysis of Porosity and Pore Structures. Reviews in Mineralogy and Geochemistry. 2015; 80(1):61–164.
53. Cavnar SP, Xiao A, Gibbons AE, Rickelmann AD, Neely T, Luker KE, Takayama S, Luker GD. Imaging Sensitivity of Quiescent Cancer Cells to Metabolic Perturbations in Bone Marrow Spheroids. Tomography: a journal for imaging research. 2016; 2(2):146–157.
54. Gaggioli C, Hooper S, Hidalgo-Carcedo C, Grosse R, Marshall JF, Harrington K, Sahai E. Fibroblast-led collective invasion of carcinoma cells with differing roles for RhoGTPases in leading and following cells. Nat Cell Biol. 2007; 9(12):1392–1400. [PubMed: 18037882]
55. Gkretsi V, Stylianou A, Stylianopoulos T. Vasodilator-Stimulated Phosphoprotein (VASP) depletion from breast cancer MDA-MB-231 cells inhibits tumor spheroid invasion through downregulation of Migfilin, β-catenin and urokinase-plasminogen activator (uPA). Experimental Cell Research. 2017; 352(2):281–292. [PubMed: 28209486]
56. Zhang W, Li C, Baguley BC, Zhou F, Zhou W, Shaw JP, Wang Z, Wu Z, Liu J. Optimization of the formation of embedded multicellular spheroids of MCF-7 cells: How to reliably produce a biomimetic 3D model. Analytical Biochemistry. 2016; 515:47–54. [PubMed: 27717854]
57. Costa ET, Camargo AA. Beyond the Proteolytic Activity: Examining the Functional Relevance of the Ancillary Domains Using Tri-Dimensional (3D) Spheroid Invasion Assay. In: Cal S, Obaya AJ, editorsProteases and Cancer: Methods and Protocols. Springer; New York, New York, NY: 2018. 155–168.
58. Orimo A, Gupta PB, Sgroi DC, Arenzana-Seisdedos F, Delaunay T, Naeem R, Carey VJ, Richardson AL, Weinberg RA. Stromal Fibroblasts Present in Invasive Human Breast Carcinomas Promote Tumor Growth and Angiogenesis through Elevated SDF-1/CXCL12 Secretion. Cell. 2005; 121(3):335–348. [PubMed: 15882617]
59. Smith MCP, Luker KE, Garbow JR, Prior JL, Jackson E, Piwnica-Worms D, Luker GD. CXCR4 Regulates Growth of Both Primary and Metastatic Breast Cancer. Cancer Research. 2004; 64(23): 8604. [PubMed: 15574767]
60. Kojima T, Moraes C, Cavnar SP, Luker GD, Takayama S. Surface-templated hydrogel patterns prompt matrix-dependent migration of breast cancer cells towards chemokine-secreting cells. Acta Biomaterialia. 2015; 13:68–77. [PubMed: 25463502]
61. Hartmann TN, Burger JA, Glodek A, Fujii N, Burger M. CXCR4 chemokine receptor and integrin signaling co-operate in mediating adhesion and chemoresistance in small cell lung cancer (SCLC) cells. Oncogene. 2005; 24(27):4462–4471. [PubMed: 15806155]
62. Engl T, Relja B, Marian D, Blumenberg C, Müller I, Beecken W-D, Jones J, Ringel EM, Bereiter-Hahn J, Jonas D, Blaheta RA. CXCR4 Chemokine Receptor Mediates Prostate Tumor Cell Adhesion through α(5) and β(3) Integrins. Neoplasia (New York, NY). 2006; 8(4):290–301.
63. Gioiella F, Urciuolo F, Imparato G, Brancato V, Netti PA. An Engineered Breast Cancer Model on a Chip to Replicate ECM-Activation In Vitro during Tumor Progression. Advanced Healthcare Materials. 2016; 5(23):3074–3084. [PubMed: 27925458]
64. Thakuri PS, Liu C, Luker GD, Tavana H. Biomaterials-Based Approaches to Tumor Spheroid and Organoid Modeling. Adv Healthc Mater. 2017
65. Erdogan B, Ao M, White LM, Means AL, Brewer BM, Yang L, Washington MK, Shi C, Franco OE, Weaver AM, Hayward SW, Li D, Webb DJ. Cancer-associated fibroblasts promote directional cancer cell migration by aligning fibronectin. The Journal of Cell Biology. 2017
66. Han W, Chen S, Yuan W, Fan Q, Tian J, Wang X, Chen L, Zhang X, Wei W, Liu R, Qu J, Jiao Y, Austin RH, Liu L. Oriented collagen fibers direct tumor cell intravasation. Proceedings of the National Academy of Sciences. 2016; 113(40):11208.
67. Rooney P, Kumar S, Ponting J, Wang M. The role of hyaluronan in tumour neovascularization (review). International Journal of Cancer. 1995; 60(5):632–636. [PubMed: 7532158]
68. Chanmee T, Ontong P, Itano N. Hyaluronan: A modulator of the tumor microenvironment. Cancer Letters. 2016; 375(1):20–30. [PubMed: 26921785]

Statement of Significance

Our manuscript describes a novel design of hybrid hydrogel system composed of collagen and alginate modeling 3D tumor environments in breast cancer. The hydrogel possesses a well-organized, homogenous microstructure with adjustable mechanical stiffness. Upon embedding tumor spheroids, we successfully showed a 3D tumor invasion model showing follow-the-leader migration with fibroblasts leading invasion of cancer cells similar to in vivo. To the best of our knowledge, this is the first study showing two spheroids invade simultaneously and forming bridge-like connection and effects of chemical gradients in 3D hydrogel environment. This research provides a new model for tumor-stromal interactions in cancer cell migration and establishes a novel hydrogel system for analyzing physical and biochemical signals regulating cancer progression and response to therapy.

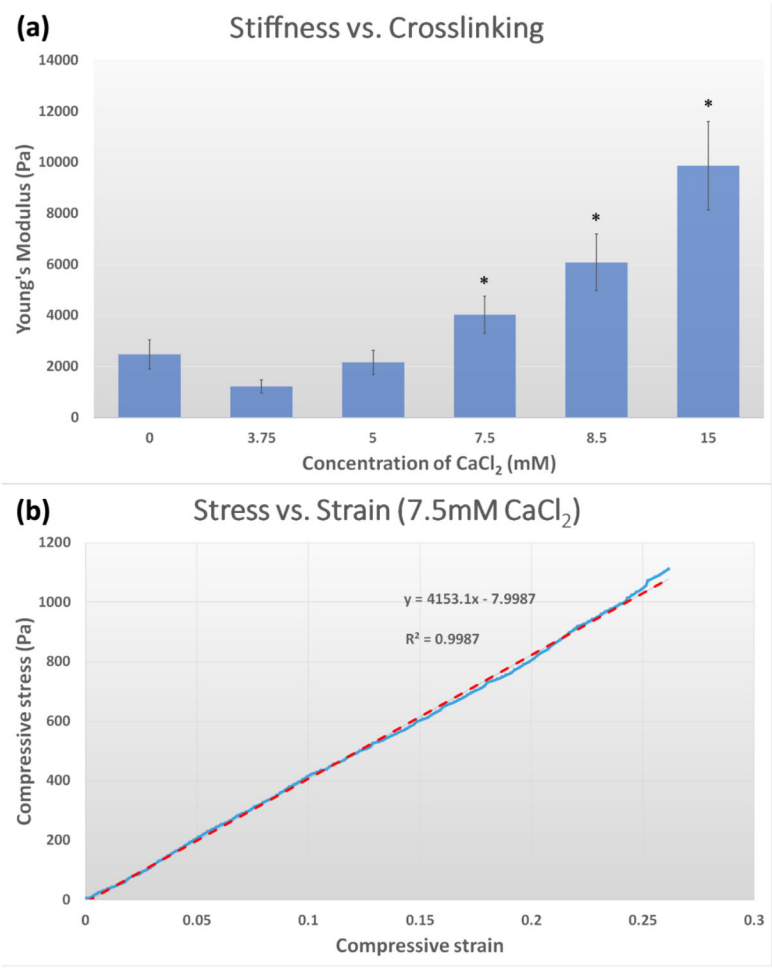

Figure 1.

Mechanical properties of Col/Algi gel. (a) Young's modulus as a function of calcium crosslinking. Data are shown as mean and standard deviation (n=6). *: $p < 0.05$. (b) Representative stress-strain curve of Col/Algi gel crosslinked at $CaCl_2$ concentration of 7.5mM.

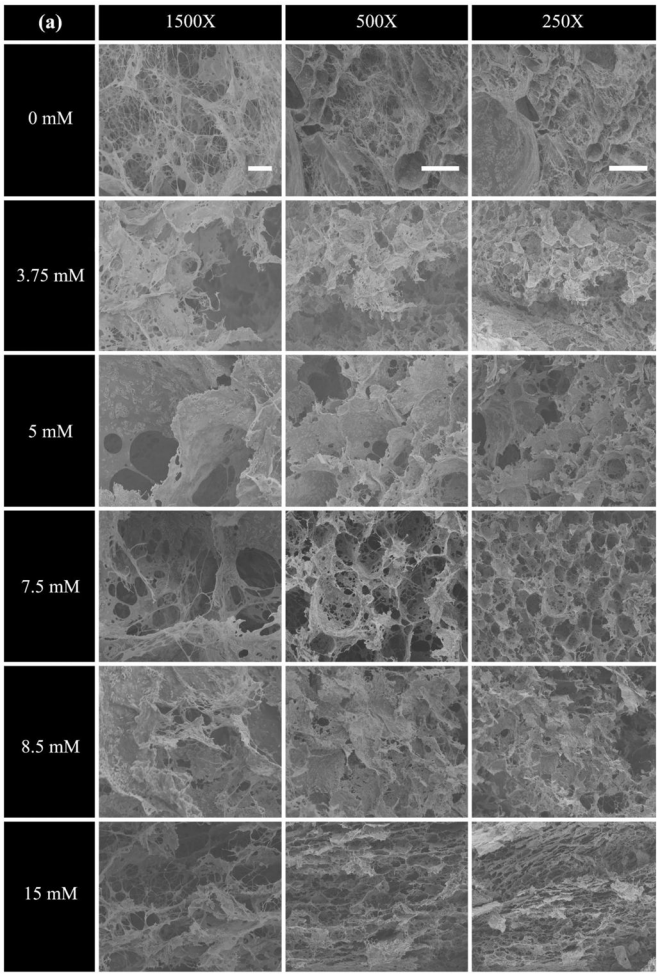

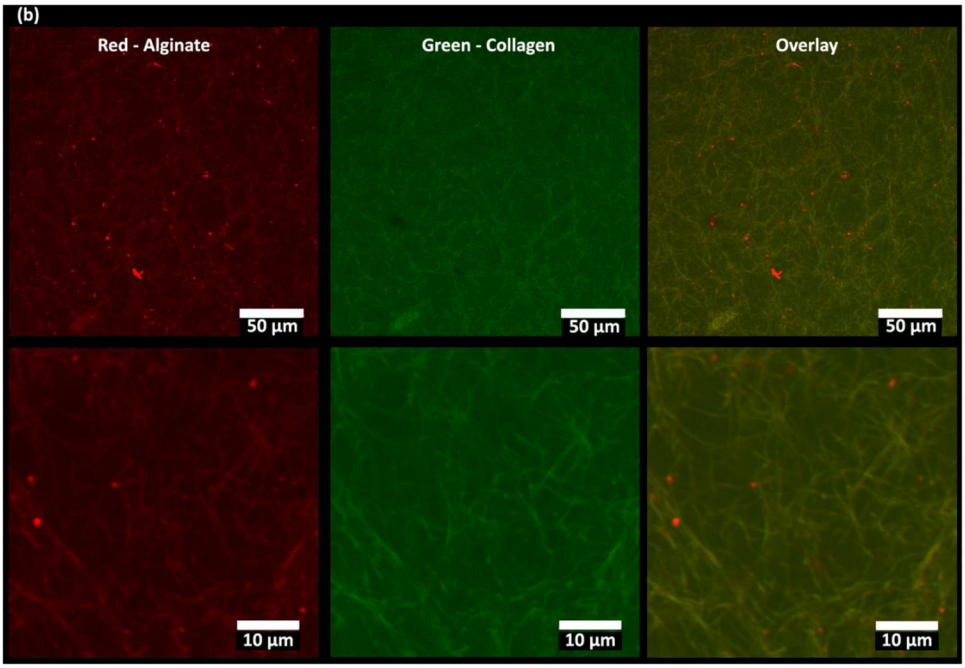

Figure 2.

Microstructure of Col/Algi gel with different concentrations of $CaCl_2$. (a) Scanning electron micrographs of Col/Algi hydrogels crosslinked at $CaCl_2$ concentrations of 0, 3.75, 5, 7.5, 8.5 and 15 mM (from top to bottom). Images were taken at magnification of 1500X (left), 500X (middle), and 250X (right). Scale bars indicate 10 μm, 50 μm, and 100 μm respectively. (b) Fluorescence images of a blank Col/Algi gel at 25X (a) and 50X (b) magnification. Red color indicates rhodamine tagged alginate molecules and green color indicates collagen fibers stained by FITC- tagged collagen binding reagent. Images are presented as maximum intensity in z-projection over a depth of 200 μm.

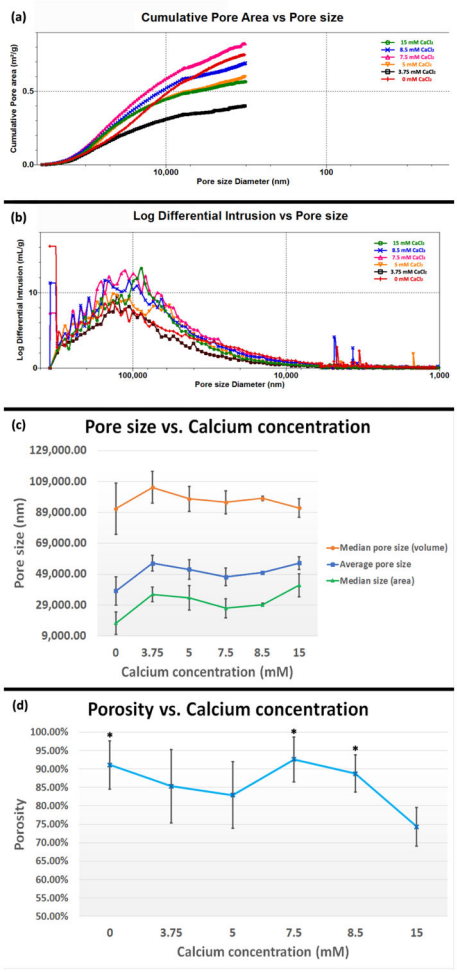

Figure 3.

Pore structure of Col/Algi gel. (a) Cumulative pore area distribution with pore size. (b) Pore size distribution of Col/Algi gel with different $CaCl_2$ concentrations. The amount of pore space for a given pore size diameter is illustrated by log differential intrusion of mercury, where peaks show pore sizes occupying the greatest amount of overall porosity. (c) Average pore size and median pore size corresponding to volume and surface area. (d) Porosity of Col/Algi gel crosslinked at different $CaCl_2$ concentrations. *: > 15 mM, $p < 0.05$. All numbers shown in (c) and (d) are weighted means and weighted standard deviations.

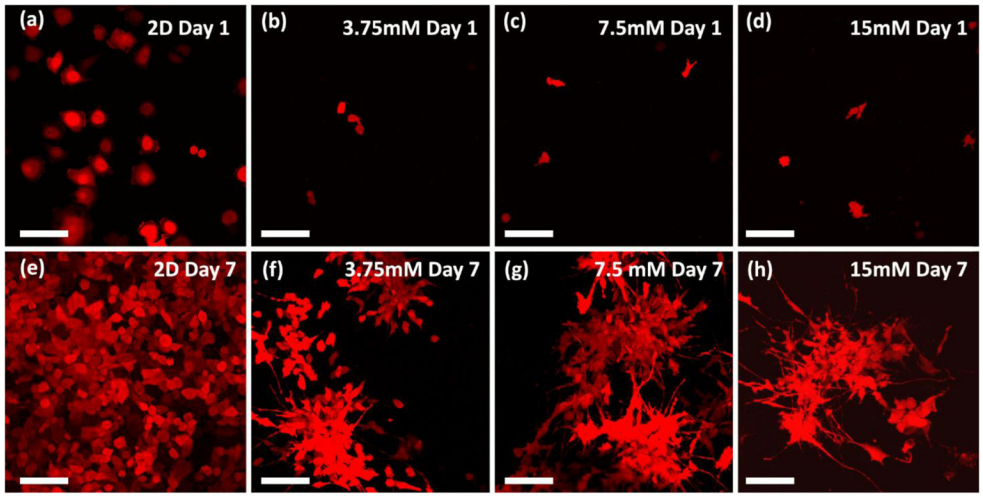

Figure 4.

Cancer cells in 3D gel environment. Images show MDA-MB-231 cells stably expressing fluorescent protein mKate (shown as red in images) in 3D gel culture for 1 day (a, b, c, and d) and 7 days (e, f, g, and h). (a, e) in 2D culture, (b, f) in 3.75mM $CaCl_2$ cross-linked hydrogel, (c, g) in 7.5mM $CaCl_2$ cross-linked hydrogel, and (d, h) in 15mM $CaCl_2$ cross-linked hydrogel. Images are displayed as maximum intensity in z-projection over a depth of 300 μm. Scale bar indicates 100 μm.

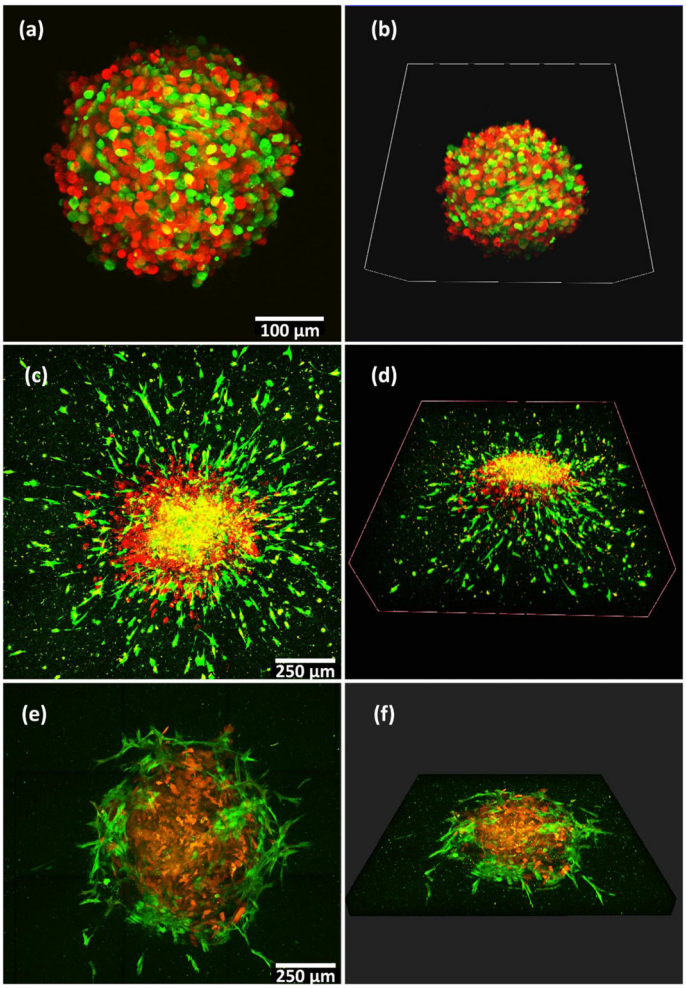

Figure 5.

Tumor spheroid invasion in 3D gel. (a–b) 231 cells and HMF cells form tumor spheroids after 48 hours in non-adherent round bottom plates (indicated as day 0 in Figure 5e). (c–d) A spheroid transferred into a 3D gel at day 0 and cultured for 6 days in the gel shows extensive invasion. (e–f) A spheroid transferred into gel containing only collagen at day 0 and cultured in the gel for 6 days shows minimal invasion only of HMF cells. For (a–f), red color illustrates MDA-MB-231 cells expressing mKate fluorescent protein and green color illustrates HMF cells expressing GFP. Left images (a, c, e) show the maximum intensity in z-projection over a depth of 300 μm, and right images (b, d, f) show the 3D structure of a spheroid.

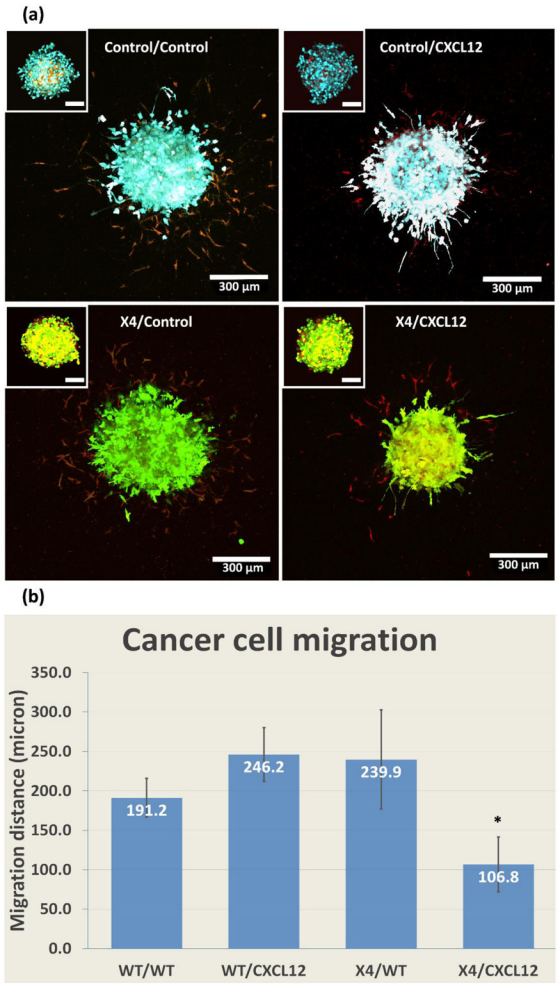

Figure 6.

CXCL12-CXCR4 signaling in 3D gel. (a) Morphologies of spheroids with HMFs secreting CXCL12 and MDA-MB-231 cells expressing CXCR4 (X4) in the 7.5 mM $CaCl_2$ hydrogel after 5 days in culture. The top left boxes show the same spheroid on day 0. As controls we used spheroids combining HMFs that do not secrete CXCL12 with MDA-MB-231 cells lacking CXCR4 (231(WT)/HMF(WT); 231(X4)/HMF(WT); and 231(WT)/HMF(CXCL12). We pseudo-colored cells as follows: HMF(CXCL12), red; HMF(WT), yellow; 231(X4), green; and 231(WT), cyan. (b) Quantification of invasion of cancer cells into the adjacent gel for all conditions. *: $p < 0.05$. Scale bars indicate 100 μm in top left boxes, and 300 μm in main figures.

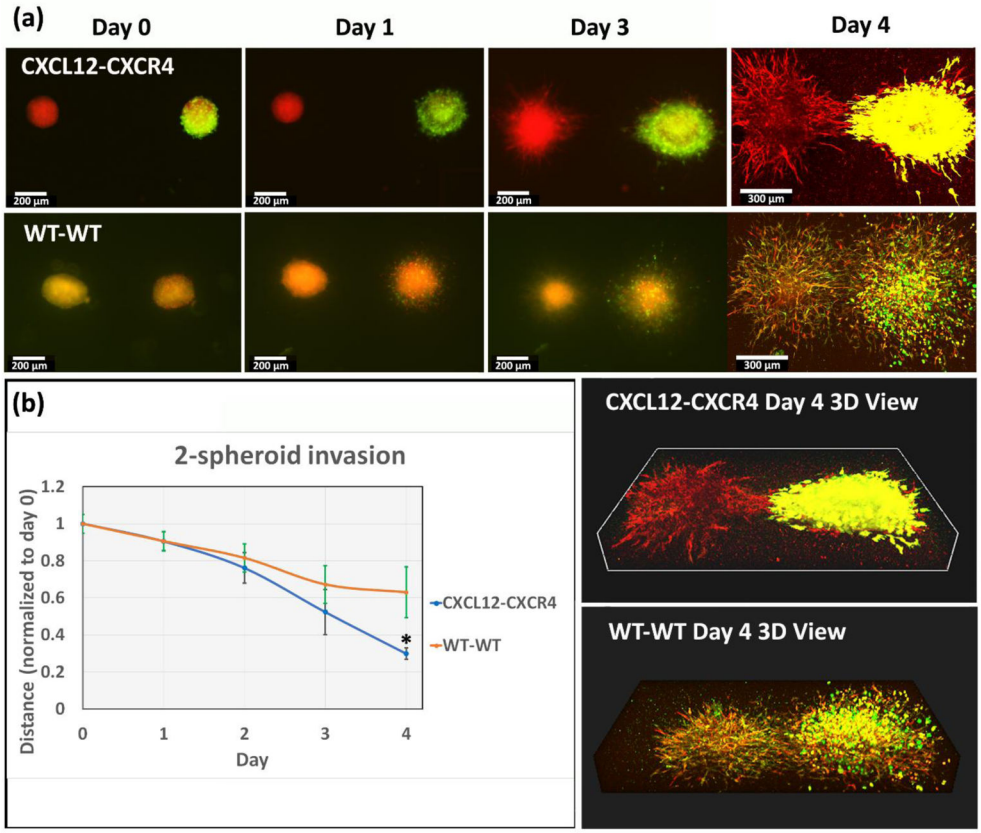

Figure 7.

CXCL12-CXCR4-driven migration between spheroids in 3D gel environment. (a) Top row: We placed spheroids of HMFs secreting CXCL12 (red fluorescence) and spheroid of MDA-MB-231 cells expressing CXCR4 (X4) (green fluorescence) and HMF wild type (red fluorescence) in the 7.5 mM $CaCl_2$ hydrogel. Bottom row: Spheroid of wild-type HMFs and spheroid of wild-type MDB-MB-231 cells and HMF wild-type were placed in the same gel. Initial separation between spheroids was ~ 1 mm. We quantified cell invasion from spheroids for 4 days. (b) Graph shows mean distances ± standard deviation from the invasion margin of cancer spheroids to the center of HMF spheroids, normalized to the initial separation on day 0, *: < WT-WT, $p < 0.05$. Scale bars indicate 200 µm in images from day 0 to day 3, and 300 µm in day 4.